



**Ciências  
ULisboa**

# **Diving in the Early Universe with Webb: the CEERS-24413 Case**

ASTROPHYSICS LABORATORY

*Diogo António Gil*

Orientador:  
Ciro Pappalardo

July 5, 2025

# Contents

<b>1</b>	<b>Introduction</b>	<b>2</b>
<b>2</b>	<b>Theoretical Background</b>	<b>3</b>
2.1	Star-Forming Galaxies and Nebular Emission . . . . .	3
2.2	The BPT Diagram and Dust Extinction . . . . .	3
2.3	Galaxy Selection and the DAWN Data Portal . . . . .	5
2.4	Overview of the FADO Tool . . . . .	5
<b>3</b>	<b>Test Galaxy Preparation</b>	<b>6</b>
3.1	Pipeline Validation on a Test Galaxy Prior to Main Sample Analysis . . . . .	6
3.2	BPT Classification . . . . .	8
<b>4</b>	<b>Main Sample Data</b>	<b>8</b>
4.1	Target Selection . . . . .	8
4.2	Spectral File Processing . . . . .	9
4.2.1	BPT Classification . . . . .	9
4.2.2	Spectral Resolution Estimation for FADO . . . . .	10
<b>5</b>	<b>Analysis with FADO</b>	<b>11</b>
5.1	Spectral Fitting Methodology . . . . .	11
5.2	Results from FADO . . . . .	11
5.3	H $\alpha$ Line Profile: Multi-Gaussian Fit . . . . .	12
5.4	Black hole Mass Estimation . . . . .	13
5.5	Model Interpretation . . . . .	14
<b>6</b>	<b>Discussion</b>	<b>15</b>
6.1	Diagnostic Diagram Validation . . . . .	15
6.2	Physical Implications . . . . .	15
<b>7</b>	<b>Conclusion</b>	<b>15</b>

# 1 Introduction

To understand the mechanisms that created the early universe, it is crucial to investigate the evolution of galaxies at high redshift (corresponding to great distances and early cosmic times). In particular, examining the star formation history, the record of how stars formed over time in a galaxy, and active galactic nuclei (AGN) activity, the energetic phenomena (like powerful jets of particles or intense radiation across the electromagnetic spectrum) around supermassive black holes, which can be inferred from the study of light, also known as spectroscopic analyses.

A spectrum is the dissection of an object’s light into its component wavelengths, revealing not only emission and absorption lines but also the continuum emission. The continuum refers to the smooth underlying distribution of flux as a function of wavelength, which is caused by the combined radiation of stars, thermal dust emission, or non-thermal processes. To restore the continuum from observational data, a baseline is typically fitted to the spectrum in regions that are free of strong lines in order to isolate the continuum from the superposed spectral features. This is both for the purposes of measuring emission-line fluxes and for constraining the physical properties of the stellar populations.

In this paper, a detailed spectroscopic analysis of a galaxy is presented, designated as 24413 by the DAWN database <sup>1</sup>, an online archive which provides public access to JWST spectroscopic observations and derived properties of galaxies observed in early release science programmes.

The object is located at right ascension 53.165314 and declination  $-27.81414$ , at a redshift of  $z = 3.063$ , and it was observed as part of the JADES-GDS-WIDE3 [15] program using JWST NIRSpec, the Near Infrared Spectrograph, which is an instrument on board JWST capable of obtaining spectra in the wavelength range 0.6–5 microns with multiple spectral resolutions.

The primary goals of this study are to classify the ionising sources in the galaxy, which helps to determine the physical processes driving the galaxy’s emission and evolution, to characterise the star formation properties, and to investigate for potential AGN activity by emission-line modelling and spectral synthesis.

The analysis involves the application of the Baldwin–Phillips–Terlevich (BPT) [11] diagnostic diagram, Gaussian line fitting of the  $H\alpha$  region, which covers the spectral wavelengths around 656.3 nm corresponding to the hydrogen alpha emission line (produced when electrons in hydrogen atoms transition from the third to the second energy level) and full spectral modelling using the FADO TOOL [1].

In star-forming galaxies and active galactic nuclei, nebular emission lines arise from ionised gas illuminated by young massive stars or the central AGN. The  $H\alpha$  emission line, produced by the transition of hydrogen electrons from the  $n=3$  to  $n=2$  energy level, is one of the strongest features in optical spectra and serves as a key tracer of star formation and ionisation conditions. From these methods, physical parameters such as the stellar mass, star formation rate (SFR), stellar age distribution, and black hole mass of the AGN are derived.

Understanding how galaxies and their supermassive black holes influence each other over time (galaxy-AGN coevolution) is one of the keys to unlocking the drivers of galaxy evolution. This galaxy-AGN coevolution regulates both star formation and black hole growth, thereby shaping the observable properties of those galaxies. To study this relationship, physicists rely on an approach that combines stellar population synthesis and emission-line diagnostics, facilitating a characterisation of the galaxy’s ionisation mechanisms and evolutionary state.

The stellar continuum is the smooth underlying radiation caused by the sum of light from the stars across various wavelengths. On top of this continuum, absorption lines appear, due to elements present in stars’ atmospheres that absorb specific wavelengths of light, and emission lines, caused by ionised gas clouds around stars or active galactic nuclei (AGN) emitting light at specific wavelengths.

---

<sup>1</sup><https://dawn.ipac.caltech.edu/>

## 2 Theoretical Background

In this section, a theoretical overview of the key concepts that make up this work is provided, with the aim of establishing a solid foundation for the reader to understand the analysis presented in the following sections.

### 2.1 Star-Forming Galaxies and Nebular Emission

Young, massive stars in star-forming galaxies release strong ultraviolet (UV) radiation that can ionise the interstellar medium (ISM) around them, creating H II regions (clouds of ionised hydrogen). On top of the stellar continuum, there are strong nebular emission lines produced when the ionised gas re-emits photons at discrete wavelengths during recombination, whether the ionisation is caused by young stars or by AGN activity.

These emission lines, especially hydrogen recombination lines, for example,  $H\alpha$  and  $H\beta$ , as well as forbidden lines like [O III]  $\lambda 5007$ , [N II]  $\lambda 6584$ , and [S II]  $\lambda\lambda 6717, 6731$ , offer important insights into the physical properties of the ionised gas. In particular, they enable the estimation of:

**Star formation rates (SFRs)** - The rate at which a galaxy forms new stars, typically measured in solar masses per year. Can be calculated through the luminosity of recombination lines like  $H\alpha$ ;

**Dust attenuation** - The quantification of the amount of dust extinction affecting the observed emission lines, typically corrected using the Balmer decrement ( $H\alpha/H\beta$ );

**Ionisation conditions** - To distinguish between different ionising sources, star formation and AGN activity, investigated through diagnostic diagrams like the BPT diagram.

Since nebular emission tracks the impact of recent star formation on the ISM, it is essential to interpret it while examining galaxy spectra.

Since nebular emission tracks the effect of new star formation on the interstellar medium (ISM), it must be included in galaxy spectrum fitting. The spectral fitting code FADO [1] models both stellar and nebular components simultaneously, providing a physically coherent fit to observed spectra of star-forming galaxies and allowing more accurate determinations of intrinsic properties such as stellar masses, ages, and star formation rates (SFRs).

### 2.2 The BPT Diagram and Dust Extinction

Tools that can separate different ionisation mechanisms and correct for dust attenuation are essential to understanding the physical conditions in star-forming galaxies. Two important diagnostic techniques used for this purpose are the BPT diagram and the Balmer decrement.

**The BPT Diagram** Proposed by Baldwin in 1981, the Baldwin–Phillips–Terlevich (BPT) diagram uses ratios of strong emission lines, typically [O III]  $\lambda 5007/H\beta$  versus [N II]  $\lambda 6584/H\alpha$ , to distinguish between ionisation caused by massive young stars and other sources such as active galactic nuclei (AGN). Theoretical (Kewley2001 [5]) and empirical (Kauffmann2003 [6]) demarcation curves define regions in this space associated with star formation, composite activity, and AGN. Because it relies on emission lines that are close in wavelength, the BPT diagram is relatively insensitive to dust extinction, since dust affects nearby wavelengths similarly; this will be explained in more detail later.

Star-forming galaxies typically lie below and to the left of the Kauffmann [6] curve, AGN-dominated galaxies lie above the Kewley [5] curve, and galaxies in between are classified as composites, indicating contributions from both star formation and AGN activity.

These line ratios reflect differences in the ionising radiation and physical conditions of the gas. The [O III]  $\lambda 5007/H\beta$  ratio measures the excitation state of the gas by comparing a high-ionisation line ([O III]) to a hydrogen recombination line ( $H\beta$ ), while the [N II]  $\lambda 6584/H\alpha$  ratio indicates the relative abundance of nitrogen and the ionisation parameter.

Massive young stars produce softer ultraviolet radiation, resulting in lower [O III]  $\lambda 5007/H\beta$  ratios, whereas the harder radiation from AGN leads to higher [O III]  $\lambda 5007/H\beta$  ratios and elevated [N II]  $\lambda 6584/H\alpha$  values due to different ionisation mechanisms and metallicities.

Figure 4 shows the BPT diagnostic diagram used to classify galaxies based on their dominant ionisation sources, separating star-forming, composite, and AGN types.

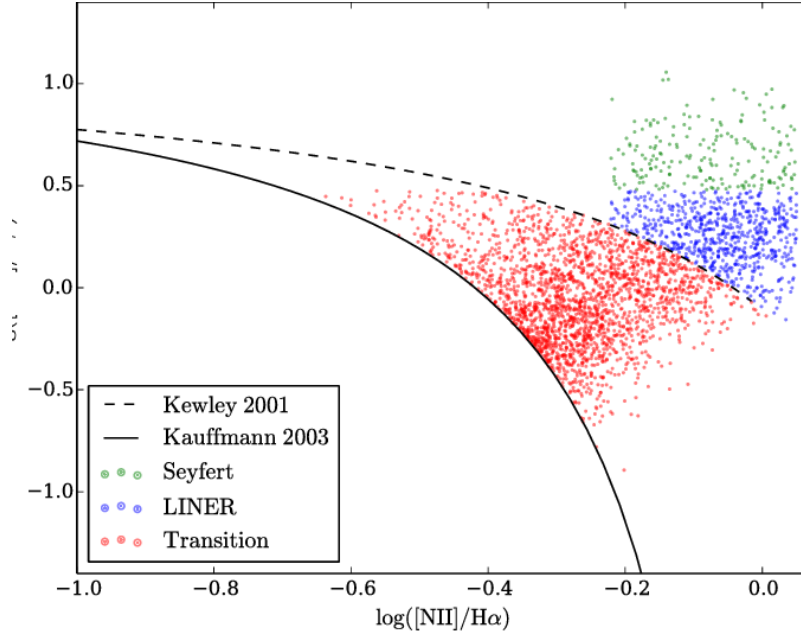


Figure 1: BPT diagnostic diagram taken from [17]. The dashed line corresponds to the theoretical maximum starburst line from Kewley [5], while the solid line shows the empirical division from Kauffmann [6]. Data points are colour-coded as follows: Seyfert galaxies (green), LINERs (blue), and transition objects (red). The galaxy studied in this paper is not shown in this diagram.

**Dust Extinction and Attenuation: The Balmer Decrement** The measured emission is attenuated because dust within galaxies absorbs and scatters stellar light, particularly at shorter wavelengths. Although the terms "extinction" and "attenuation" are sometimes used interchangeably, they refer to distinct processes. While attenuation accounts for the overall impact across several sightlines within galaxies, including scattering back into the line of sight and the existence of unobscured regions, extinction describes the absorption and scattering of light along a single line of sight (for example, towards a star).

In practice, attenuation is computed using empirical or theoretical attenuation curves by comparing observed spectra to dust-free models, similarly to extinction. Examples of frequently used laws, for the attenuation curves, are the two-component model of Charlot and Fall [3], which distinguishes between young and old stellar populations; the Milky Way and Magellanic Clouds curves (Cardelli [2]; Gordon and Clayton) and the Calzetti law [4].

The Balmer decrement, defined as the flux ratio of  $H\alpha$  to  $H\beta$ , is the basis of a standard correction method for nebular emission lines. Under Case B recombination, which assumes that all Lyman-series photons are absorbed and re-emitted within the nebula, the intrinsic ratio is 2.86 (for  $T_e = 10^4$  K,  $n_e = 100 \text{ cm}^{-3}$ ) [16]. Deviations from this value indicate dust reddening, attenuation of light caused by interstellar dust, which dims and reddens the observed spectra, allowing the calculation of the colour excess  $E(B - V)$  via:

$$E(B - V) = \frac{\log(R_{\text{obs}}/2.86)}{0.4[k(H\beta) - k(H\alpha)]}, \quad (1)$$

where  $R_{\text{obs}}$  is the observed  $H\alpha/H\beta$  ratio and  $k(\lambda)$  characterises the extinction curve. This correction is essential for retrieving intrinsic luminosities and accurately estimating star formation rates (SFRs).

Once the colour excess  $E(B - V)$  is determined, the observed flux of each emission line can be corrected to its intrinsic (dust-free) value using:

$$F_{\text{int}} = F_{\text{obs}} \times 10^{0.4 k(\lambda) E(B - V)},$$

where  $F_{\text{obs}}$  is the measured flux, and  $k(\lambda)$  is the value from the adopted extinction curve at the wavelength of the line.

For a better understanding of star-forming galaxies' nature and the physical mechanisms responsible for their emission, particular attention was given to the paper [7]. This work highlights the importance of accounting for the nebular continuum when modelling the spectral energy distribution (SED) of a galaxy (specially at a low redshift).

This work also demonstrates that for typical SDSS star-forming galaxies, the inclusion of the nebular continuum has an insignificant effect on the derived star formation rate and stellar masses. However it also indicates that

perhaps this is not the case for higher redshift systems whose ionised gas contribution is expected to be greater. This finding is particularly relevant because how of much this work’s focus is on the analysis of galaxies at higher redshift, where nebular emission can significantly affect the interpretation of spectral data. This reinforces the relevance of using physically consistent modelling tools like FADO [1] when interpreting the emission of galaxies, particularly in regimes where nebular emission becomes significant.

## 2.3 Galaxy Selection and the DAWN Data Portal

The JADES (JWST Advanced Deep Extragalactic Survey) offers high-level science products on the DAWN website. Used to examine a vast catalogue of galaxies at different redshifts using the reduced and calibrated spectra it hosts from JWST/NIRSpec.

It is possible to filter the catalogue using several selection criteria (as described in Section 4.1), including redshift, signal-to-noise ratio, emission line luminosities, and data quality flags. Used to obtain the `.spec.fits` files, which feature one-dimensional extracted spectra from NIRSpec grisms, for each entry, which corresponds to a particular galaxy observation (or position).

The website was utilised to choose a galaxy with several observational entries for this study (as also described in Section 4.1), guaranteeing that the chosen source was sufficiently well-observed and had important spectral properties. The filters used in the selection process guaranteed good signal-to-noise spectra, making them appropriate for spectral analysis and modelling later on.

## 2.4 Overview of the FADO Tool

FADO [1] (Fitting Analysis using Differential Evolution Optimisation) is a state-of-the-art stellar population synthesis (SPS) tool designed to model galaxy spectra and derive their physical and evolutionary properties. It employs a self-consistent approach to fit both stellar and nebular components of optical spectra, ensuring consistency between ionising radiation and observed nebular emission. The main characteristics that enables FADO [1] to ensure that the various stellar components are consistent are:

**Differential Evolution Optimization** - Robust fitting of spectra through evolutionary algorithms.

**Nebular Consistency** - Self-consistent treatment of nebular characteristics, including  $H\alpha$ ,  $H\beta$  luminosities, and continuum near Balmer/Paschen jumps.

**Physical Properties** - Derives star formation history (SFH), stellar mass, metallicity, dust/gas properties, and electron density/temperature.

**Modular Workflow** - Three-phase process—spectra preparation, execution, and output analysis.

FADO [1] combines essential simple ingredients to generate galaxy spectra. It starts with Simple Stellar Populations (SSPs), which are clusters of stars that share similar patterns of abundance, metallicity, and age (the model’s fundamental ingredients). Then examines the star formation history and chemical evolution, comprising the evolution of stellar populations over time, along with metal enrichment variations and star formation rates.

It also incorporates dust effects by simulating both emission (reradiation of absorbed energy in the infrared) and attenuation (absorption and scattering of light by dust). These pieces together allow for observed galaxy spectra to be reconstructed in a scientifically valid way.

### Input and Execution

Observed spectra must be redshift-corrected (as described in Section 4.2) and formatted as a `.txt` file (with the respective columns, wavelength, flux, and flux error). To run FADO [1] for a single galaxy:

```
./FADO -i [spectrum_path] -b [SSP_library] -s [spectral_range] -r [resolution] -d [distance_Mpc]
```

## Output Files

FADO generates four key outputs:

- **1D**: Best-fit total, stellar, and nebular models.
- **ST**: Galaxy properties (mass, age, metallicity).
- **EL**: Emission-line measurements.
- **DE**: Properties of individual SSPs in the best-fit model.

The input spectrum and the best-fitting models (the overall spectrum and its distinct stellar and nebular components) are included in the **1D** file. The **ST** file contains the galaxy’s physical characteristics, such as stellar mass, age, and metallicity. The **EL** file offers comprehensive measurements of 51 emission lines for emission line analysis, which is essential for characterising the ionised gas component. The **DE** file contains the population vector detailing the individual SSPs that make up the best-fitting model, offering insight into the galaxy’s stellar population composition.

## 3 Test Galaxy Preparation

Before analysing the full sample, the analysis pipeline was validated on the galaxy CEERS-1345-7975 (Figure 2), which was observed with JWST/NIRSpec. This galaxy is located at a redshift of  $z = 2.74$ . The signal-to-noise ratio (S/N) of the  $H\alpha$  emission line is approximately 10.

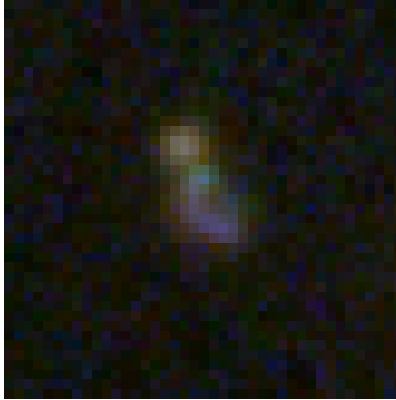


Figure 2: The galaxy CEERS-1345-7975 observed with JWST using the F115W filter. The image, taken from the DAWN website, is a single-filter observation rather than a composite.

### 3.1 Pipeline Validation on a Test Galaxy Prior to Main Sample Analysis

To begin, the observed spectra were shifted to the rest-frame by applying the relation

$$\lambda_{\text{rest}} = \frac{\lambda_{\text{observed}}}{1 + z},$$

where  $z = 2.74$  is the redshift of the source. Additionally, the observed flux densities were multiplied by  $(1 + z)$  to conserve integrated fluxes in the rest-frame.

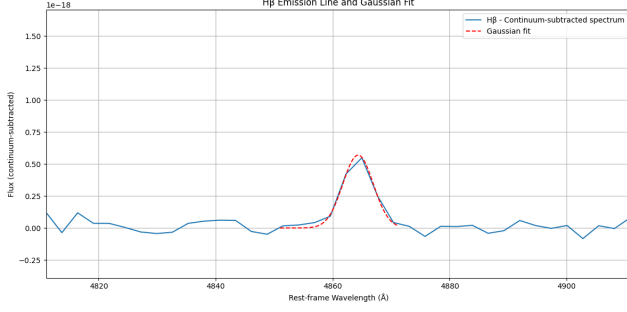
For each emission line, the continuum level was estimated by defining two sidebands on either side of the expected central wavelength in the rest-frame spectrum: one interval from  $-40 \text{ \AA}$  to  $-25 \text{ \AA}$  and another from  $+25 \text{ \AA}$  to  $+40 \text{ \AA}$  relative to the line center. The mean flux density in each sideband was computed, and the continuum was set as the average of these two mean values. This continuum level was subtracted across the full wavelength interval around the line.

After continuum subtraction, a single-component Gaussian profile was fitted to each line within a  $\pm 10 \text{ \AA}$  window centered on the rest-frame wavelength. The fit was performed using a least-squares optimisation procedure and yielded three parameters: the amplitude  $A$  (peak flux density above the continuum), the central wavelength  $x_0$ ,

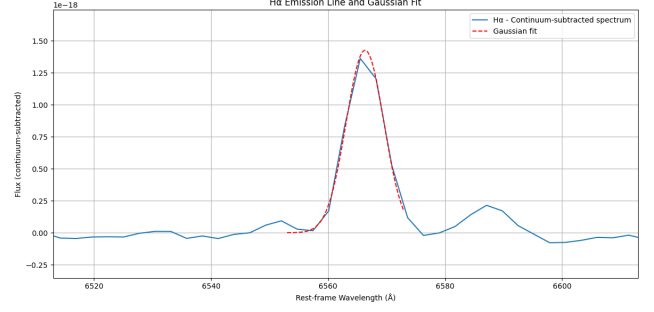
and the standard deviation  $\sigma$ . The Full Width at Half Maximum (FWHM) was computed from the best-fit  $\sigma$  using the relation:

$$\text{FWHM} = 2\sqrt{2\ln 2}\sigma \approx 2.355\sigma.$$

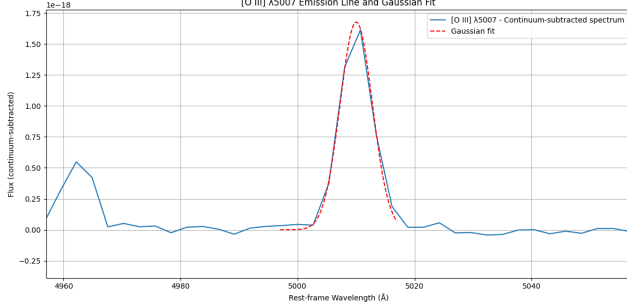
For instance, the fit to the  $\text{H}\beta$  emission line resulted in  $A = 5.69 \pm 0.57 \times 10^{-19} \text{ erg s}^{-1} \text{ cm}^{-2} \text{ \AA}^{-1}$  and  $\sigma = 2.60 \text{ \AA}$ , corresponding to a FWHM of  $6.1 \text{ \AA}$ . Similarly, for  $\text{H}\alpha$ , the fit yielded  $A = 1.43 \pm 0.14 \times 10^{-18} \text{ erg s}^{-1} \text{ cm}^{-2} \text{ \AA}^{-1}$  and  $\sigma = 3.22 \text{ \AA}$  (FWHM =  $7.6 \text{ \AA}$ ). These fits, along with the continuum-subtracted spectra, are shown in Figure 3b and 3a.



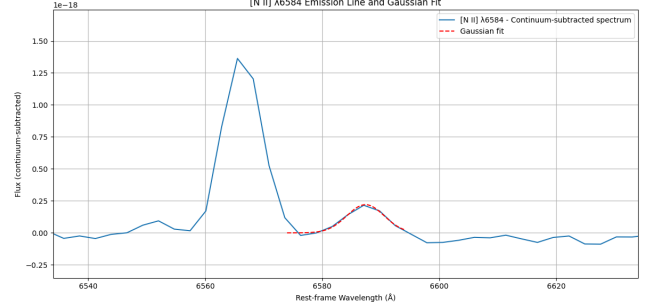
(a)  $\text{H}\beta$  line fit



(b)  $\text{H}\alpha$  line fit



(c)  $[\text{O III}] \lambda 5007$  line fit



(d)  $[\text{N II}] \lambda 6584$  line fit

Figure 3: Gaussian fits for the four emission lines.

The measured Balmer decrement  $\text{H}\alpha/\text{H}\beta = 3.11 \pm 0.31$  indicates that dust is absorbing more of the shorter wavelength  $\text{H}\beta$  photons relative to  $\text{H}\alpha$ , due to their higher susceptibility to extinction. Under standard conditions (Case B recombination at  $T_e = 10^4 \text{ K}$  and  $n_e = 100 \text{ cm}^{-3}$ ), the theoretical ratio is 2.86. A measured value of 3.11, slightly above this, corresponds to modest dust attenuation. The Calzetti extinction law [4] was used to estimate the colour excess  $E(B - V)$ .

$$E(B - V) = \frac{\log(R_{\text{obs}}/2.86)}{0.4(k_{\text{H}\beta} - k_{\text{H}\alpha})} \quad (2)$$

where  $k(\lambda) = (\lambda/5500 \text{ \AA})^{-0.7}$ . This results in a colour excess  $E(B - V) = 0.176$ . Using a typical value of  $R_V = 3.1$ , this corresponds to a visual extinction

$$A_V = R_V \times E(B - V) \approx 3.1 \times 0.176 = 0.55 \text{ mag},$$

which is consistent with FADO's attenuation estimate of  $\Delta A_V < 0.2 \text{ mag}$  within uncertainties.

The dust-corrected  $\text{H}\alpha$  luminosity is calculated using

$$L_{\text{H}\alpha} = 4\pi d_L^2 \times F_{\text{corr}}$$

where  $d_L$  is the luminosity distance (in cm) corresponding to the redshift  $z = 2.74$  and  $F_{\text{corr}}$  is the dust-corrected flux. This results in

$$L_{\text{H}\alpha} = 1.33 \times 10^{42} \text{ erg s}^{-1}$$



The star formation rate (SFR) is then estimated by applying the relation from Kennicutt [8], which links the  $H\alpha$  luminosity to the SFR as

$$\text{SFR} (M_{\odot} \text{ yr}^{-1}) = 7.9 \times 10^{-42} \times L_{H\alpha} (\text{erg s}^{-1})$$

This formula assumes a Salpeter initial mass function (IMF) over the mass range  $0.1\text{--}100 M_{\odot}$  and solar metallicity.

$$\text{SFR} = 4.33 M_{\odot} \text{ yr}^{-1} \quad (3)$$

This is consistent with the UV+IR-based SFR estimate of  $4.1 \pm 0.8 M_{\odot} \text{ yr}^{-1}$  from CEERS DR1 [12].

### 3.2 BPT Classification

It was employed the Baldwin-Phillips-Terlevich (BPT) diagnostic diagram, using the line ratios:

- $\log([\text{O III}]/\text{H}\beta) = 0.43 \pm 0.05$
- $\log([\text{N II}]/\text{H}\alpha) = -0.83 \pm 0.07$

These values (Figure 4) position the galaxy well within the star-forming region of the BPT diagram, below both the Kauffmann [6] and Kewley [5] demarcation curves. This suggests that photoionisation by young massive stars is the dominant source of nebular emission, with no evidence for AGN contribution.

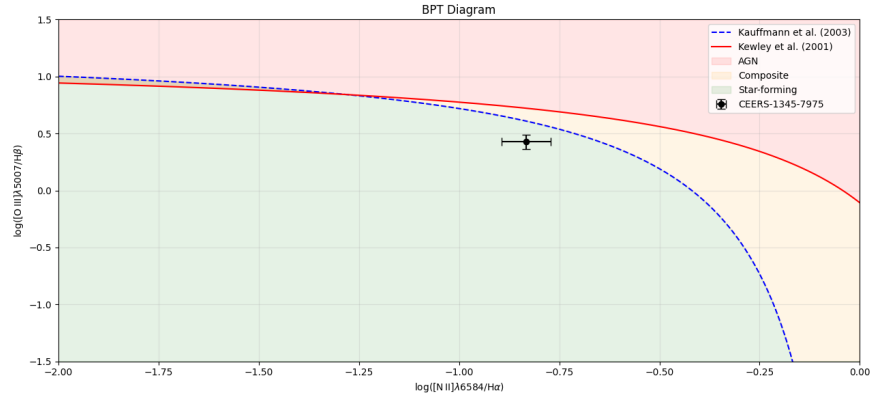


Figure 4: BPT diagnostic diagram showing the position of CEERS-1345-7975 (black circle with error bars of  $\pm 0.061$  dex in both axes). The blue dashed curve corresponds to the empirical Kauffmann [6] division, and the red solid curve is the theoretical maximum starburst line from Kewley [5]. Regions are shaded according to classification: star-forming (green), composite (orange), and AGN (red).

## 4 Main Sample Data

The galaxy used in this study was selected from the JADES catalogue using the DAWN database. The selection procedure aimed to find galaxies observed at multiple pointings to ensure greater spectral coverage and resolution.

### 4.1 Target Selection

A galaxy with two mid-resolution observations was chosen from among those with several entries (**Galaxy ID = 24413**). To guarantee high-quality data and the presence of strong emission lines, the following selection criteria were applied on the DAWN website:

- `grade == 3`: High-quality data;
- `nGr > 0`: Availability of grism spectroscopy;
- `sn50 > 50`: High signal-to-noise ratio;

- $L_{\text{H}\alpha} > 42$ : Strong  $\text{H}\alpha$  luminosity.

After applying these criteria, approximately 18 galaxies remained, including the one selected for this analysis.

## 4.2 Spectral File Processing

The selected `.fits` files were downloaded and converted into a format compatible with FADO’s input requirements for spectral fitting. A custom Python script was used to carry out the following preprocessing steps:

- Read every `.fits` file using the `astropy.io.fits` library;
- Converted observed wavelengths from microns to Ångströms;
- Corrected all spectra to rest-frame wavelengths assuming a common redshift of  $z = 3.06$ , by dividing the observed wavelengths by  $(1 + z)$ ;
- Converted flux densities from  $\mu\text{Jy}$  to physical units of  $\text{ergs}^{-1}\text{cm}^{-2}\text{\AA}^{-1}$  by computing  $f_\lambda = \frac{f_\nu c}{\lambda^2}$ ;
- Applied the redshift correction to flux (multiplied by  $1 + z$ );
- Removed invalid or duplicate data points;
- Merged all cleaned spectra into a wavelength-sorted text file for input into FADO;
- The final preprocessed spectrum is shown in Figure 5.

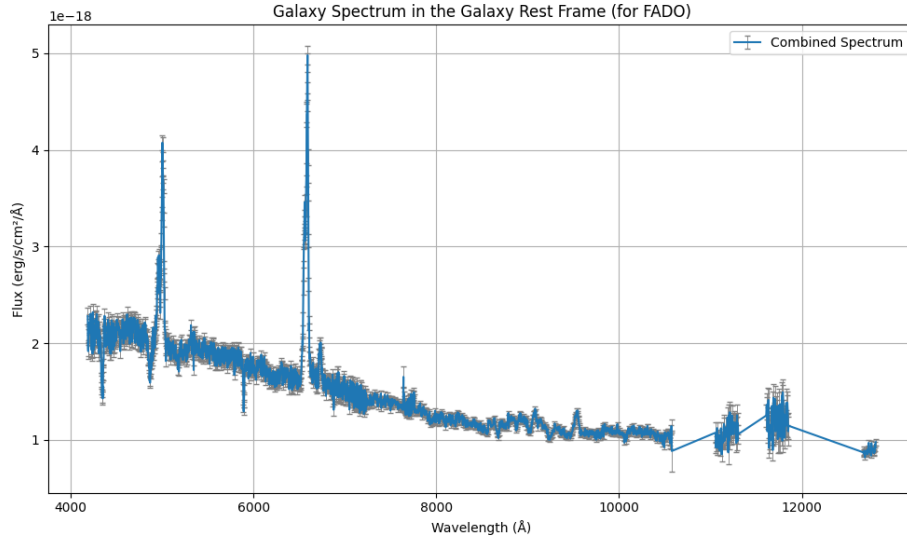


Figure 5: Combined rest-frame spectrum of galaxy 24413.

### 4.2.1 BPT Classification

It was employed the Baldwin-Phillips-Terlevich (BPT) diagnostic diagram, using the line ratios:

- $\log([\text{O III}]\lambda 5007/\text{H}\beta) = 0.277 \pm 0.03$
- $\log([\text{N II}]\lambda 6584/\text{H}\alpha) = -0.082 \pm 0.04$

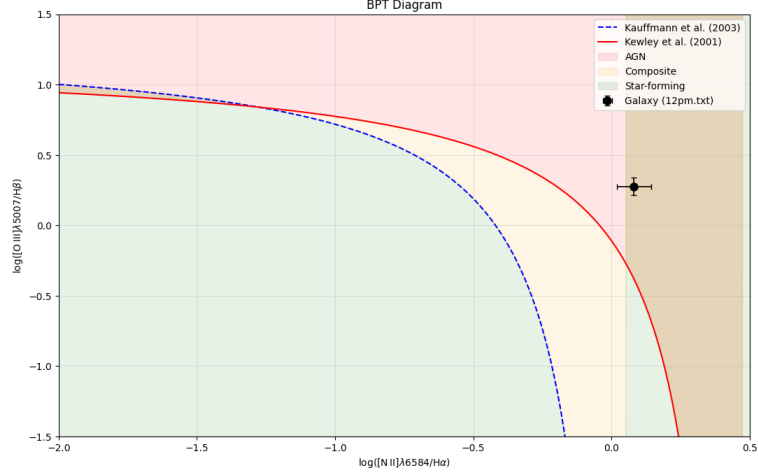


Figure 6: BPT diagnostic diagram showing the position of 24413 (black circle). The blue dashed curve corresponds to the empirical Kauffmann [6] division, and the red solid curve is the theoretical maximum starburst line from Kewley [5]. Regions are shaded according to classification: star-forming (green), composite (orange), and AGN (red).

It is visible that the galaxy (Figure 6) is positioned above the demarcation curve of Kewley [5] and firmly within the AGN zone of the BPT diagram. This suggests that active galactic nucleus activity, rather than star formation, is the main driver of ionisation in the galaxy’s nebular emission. The measured emission line ratios are strongly influenced by the presence of an AGN, indicating that non-stellar ionising sources are the main contributors.

#### 4.2.2 Spectral Resolution Estimation for FADO

To correctly set the -r parameter in FADO, it is necessary to provide the spectral resolution expressed as the ratio between the wavelengths observed and the wavelengths interval ( $\Delta\lambda$ ). The resolution affects how the synthetic spectra are adjusted to match the observed data, ensuring consistent comparison between model and observation.

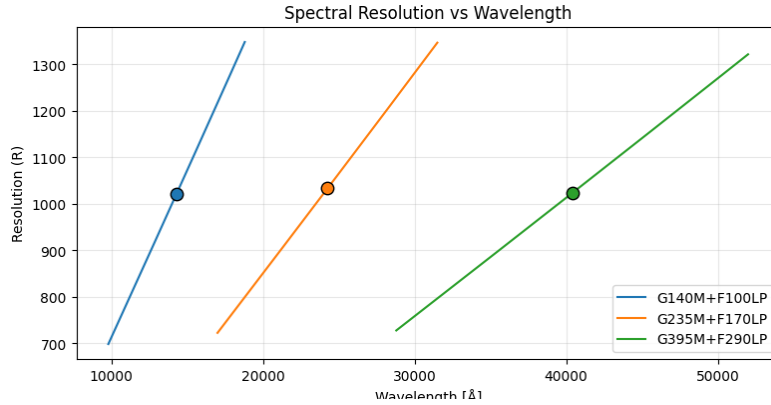


Figure 7: Spectral resolution ( $R = \lambda/\Delta\lambda$ ) as a function of wavelength for the three grating+filter combinations: G140M+F100LP, G235M+F170LP, and G395M+F290LP. The dots represent the central wavelength and mean resolution for each grism.

Table 1: Mean spectral resolution and corresponding  $\Delta\lambda$  for each grating+filter configuration, calculated using the observed-frame resolution  $R = \lambda/\Delta\lambda$  and converted to the rest-frame using  $z = 3.06$ .

Col. 1	Col. 2	Col. 3	Col. 4	Col. 5
Grating+Filter	$\lambda_{\text{mean}}$ [Å]	$R_{\text{mean}}$	$\Delta\lambda_{\text{rest}}$ [Å]	$\Delta\lambda_{\text{step}}$ [Å]
G140M+F100LP	14300.00	1021.83	3.45	1.72
G235M+F170LP	24252.19	1033.23	5.78	2.89
G395M+F290LP	40395.29	1023.40	9.72	4.86

The columns are as follows:

- Col. 1 - indicates the grating and filter configuration used in the observation.
- Col. 2 - is the mean observed-frame wavelength of the configuration in Ångströms.
- Col. 3 - gives the mean spectral resolution  $R$ , defined as  $R = \lambda/\Delta\lambda$  in the observed frame.
- Col. 4 - shows the rest-frame resolution element  $\Delta\lambda_{\text{rest}}$ , computed by correcting the observed resolution for the galaxy's redshift ( $z = 3.06$ ).
- Col. 5 - ( $\Delta\lambda_{\text{step}}$ ) represents the wavelength interval between consecutive data points in the spectrum.

Using the relation  $R = \lambda/\Delta\lambda$ , and by converting to the restframe, the  $\Delta\lambda$  resulting values are 3.45 Å for G140M+F100LP, 5.78 Å for G235M+F170LP, and 9.72 Å for G395M+F290LP, as shown in Table 1 and Figure 7.

## 5 Analysis with FADO

### 5.1 Spectral Fitting Methodology

The spectral synthesis of the galaxy was performed using the FADO [1], using the command:

```
./FADO -i input/12pm.txt -o output1x -b SPPs/Base.BC03.L -s 2500 10000 2 -r 1.8 -d 26035.44
```

Where:

- **-s** limits the wavelength fitting range to 2500–10000 Å;
- **-r** gives the spectral resolution in Ångströms (1.8 Å);
- **-d** is the luminosity distance in Mpc ( $d_L = 26035.44$  Mpc). This was estimated using the **Astropy** package with the **FlatLambdaCDM** cosmological model, assuming  $H_0 = 70 \text{ km s}^{-1} \text{ Mpc}^{-1}$ ,  $\Omega_m = 0.3$ , and the dark energy density  $\Omega_\Lambda$ ,  $1 - \Omega_m$ .

### 5.2 Results from FADO

The FADO [1] fitting output is shown in Figure 8, which includes the stellar continuum fitting, emission-line modelling, and star formation history reconstruction. From this analysis, we extract key physical parameters of the galaxy.

- Instantaneous star formation rate:  $\log(\text{SFR}_0) = -0.9482 \Rightarrow \text{SFR}_0 \approx 0.112 M_\odot \text{ yr}^{-1}$ , estimated from the mass formed in the youngest stellar population derived by FADO.
- Mean star formation rate:  $\log\langle\text{SFR}\rangle = -1.0588 \Rightarrow \langle\text{SFR}\rangle \approx 0.088 M_\odot \text{ yr}^{-1}$ , calculated as the total stellar mass formed divided by the light-weighted mean stellar age obtained from FADO.
- Stellar mass:  $\log M_\star = 8.2898 \Rightarrow M_\star \approx 1.94 \times 10^8 M_\odot$ , taken directly from FADO results.
- Light-weighted age:  $\langle\log t_\star\rangle_L = 8.777$ , representing the mean stellar age weighted by the light contribution, also provided by FADO.
- Extinction (nebular):  $A_V^{\text{neb}} = 0.2845 \text{ mag}$ .

It is important to note that the instantaneous and mean star formation rates are not directly output by FADO but were derived from the star formation history reconstruction, using the SSP mass weights and their respective ages provided by the code.

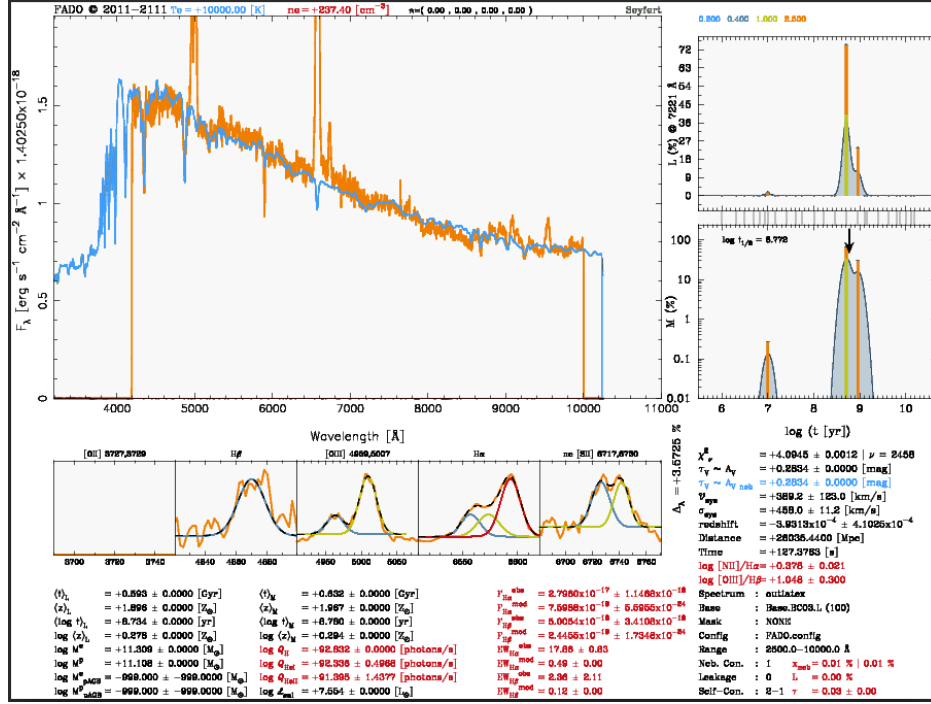


Figure 8: Output from the FADO [1] spectral synthesis model. The figure displays the measured spectrum (orange), and the fitted spectrum (blue).

### 5.3 H $\alpha$ Line Profile: Multi-Gaussian Fit

To investigate the ionised gas kinematics in greater detail, the H $\alpha$  emission region was modelled using a four-component Gaussian fit. Four components were used to separate the narrow and broad H $\alpha$  lines and the two [N II] lines, which overlap closely in wavelength. While the FADO [1] code provides a global view of the stellar and nebular emission, although it does resolve individual line shapes, the AGN change the shape of the lines. This spectral decomposition enables the identification of broad emission features, typically associated with the presence of an active galactic nucleus (AGN), because broad lines come from a fast-moving gas near the supermassive black hole in an AGN, causing Doppler broadening.

The observed spectrum in the rest-frame range 6480–6640 Å was fitted with four Gaussian components: a narrow H $\alpha$  core, a broad H $\alpha$  wing, and the [N II] doublet at 6548.88 Å and 6584.00 Å.

A constant continuum level was also included. All fluxes were normalised to a factor of  $1 \times 10^{-18} \text{ erg s}^{-1} \text{ cm}^{-2} \text{ Å}^{-1}$  for clarity.

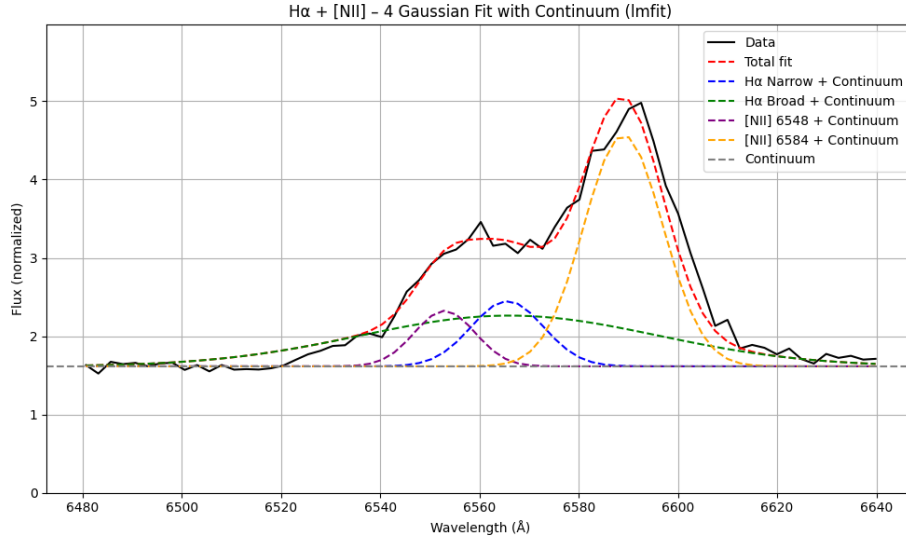


Figure 9: Decomposition of the H $\alpha$  line region using a four-Gaussian fit plus constant continuum. The observed spectrum (black) is well matched by the total model (red dashed line). The individual Gaussian components correspond to: narrow H $\alpha$  (blue), broad H $\alpha$  (green), [N II] 6548 (purple), and [N II] 6584 (orange), each overlaid with the continuum. The continuum level is shown as a grey dashed line. The wavelength range has been extended to improve visual clarity.

The asymmetric and extended red wing of the H $\alpha$  profile is well captured by the broad Gaussian component, with a best-fit full width at half maximum (FWHM) of  $\sim 3228 \text{ km s}^{-1}$ . This broad emission is a robust indicator of an AGN-driven origin, as typical star-forming regions rarely reach such velocities; typical star-forming regions have emission line widths (FWHM) of a few hundred km/s, usually below 300 km/s. The inclusion of the [N II] lines was essential to isolate the true broad H $\alpha$  contribution and avoid flux overestimation.

The fit is an excellent representation of the data, with  $R^2 = 0.97$  and reduced chi-square of  $\chi_u^2 = 0.032$ , confirming the model's adequacy. Some parameters (e.g., `mu2`, `sigma2`) reached boundary values, which may reflect either physical limits (e.g., maximum plausible broadening) or a need for further exploration of parameter space.

## SFR Estimation from H $\alpha$ Luminosity

The narrow component refers to the Gaussian component with smaller width ( $\sigma$ ) centered at the H $\alpha$  wavelength (6563 Å) in the multi-Gaussian fit. It is explicitly shown in the figure of the fit, blue dashed line in Figure 9.

The H $\alpha$  luminosity from the narrow component is given as:

$$\log L_{\text{H}\alpha, \text{n}} = 40.0595 \Rightarrow L_{\text{H}\alpha} = 10^{40.0595} \text{ erg/s}$$

The SFR can be estimated from the H $\alpha$  luminosity using the Kennicutt [8] calibration:

$$\text{SFR}_{\text{H}\alpha} [M_{\odot} \text{ yr}^{-1}] = 7.9 \times 10^{-42} \times L_{\text{H}\alpha} [\text{erg s}^{-1}]$$

$$\text{SFR}_{\text{H}\alpha} = 7.9 \times 10^{-42} \times L_{\text{H}\alpha}$$

Substituting the values:

$$\text{SFR}_{\text{H}\alpha} = 7.9 \times 10^{-42} \times 1.15 \times 10^{40} \approx 0.0908 M_{\odot} \text{ yr}^{-1}$$

## 5.4 Black hole Mass Estimation

Using the broad H $\alpha$  component from the fit, the black hole mass ( $M_{\text{BH}}$ ) was estimated via the virial method [13]. This method [13] estimates the black hole mass assuming the broad-line region gas is virialised, using the width of broad emission lines and luminosity as proxies for velocity and size. The derived properties are:

$$\text{FWHM}_{\text{H}\alpha, \text{broad}} = 3228 \text{ km s}^{-1}, \quad L_{\text{H}\alpha, \text{broad}} = 4.14 \times 10^{42} \text{ erg s}^{-1}.$$

Applying the scaling relation from Greene [9]:

$$M_{\text{BH}} = 2.0 \times 10^6 \left( \frac{L_{\text{H}\alpha}}{10^{42} \text{ erg s}^{-1}} \right)^{0.55} \left( \frac{\text{FWHM}_{\text{H}\alpha}}{10^3 \text{ km s}^{-1}} \right)^{2.06},$$

yields an estimated mass of:

$$M_{\text{BH}} \approx 4.55 \times 10^7 M_{\odot}.$$

This mass is consistent with typical Type 1 AGNs at similar redshifts ( $z \sim 3$ ) [14] and reinforces the classification of the source as an AGN-dominated system.

## 5.5 Model Interpretation

To further contextualise the properties of the galaxy, its star formation rate (SFR) and stellar mass ( $M_{\star}$ ) is compared to the empirical star-forming "main sequence" (MS) derived from local galaxies. This relation reflects a tight correlation between stellar mass and star formation activity, and galaxies that deviate from it are often experiencing quenching or enhanced starburst phases.

The reference main sequence adopted here is taken from Speagle [10], evaluated at  $z \sim 3.06$ , corresponding to a Universe age of  $t \sim 2.07$  Gyr. The parameterisation is:

$$\log \text{SFR}_{\text{MS}} = a(t) \log M_{\star} + b(t),$$

$$\text{with } a(t) = 0.84 - 0.026t, \quad b(t) = -(6.51 - 0.11t),$$

which yields, for  $t = 2.07$ :

$$\log \text{SFR}_{\text{MS}} \approx 0.484 \log M_{\star} - 5.997.$$

From the FADO [1] stellar population synthesis and the  $\text{H}\alpha$  emission line analysis (the narrow  $\text{H}\alpha$  component flux only, as it better traces star formation with less contamination from the AGN broad component), we adopt  $\log(\text{SFR}_{\text{H}\alpha}) = -1.04$  and  $\log M_{\star} = 8.29$ . These values are plotted in Figure 10, together with the main sequence curve.

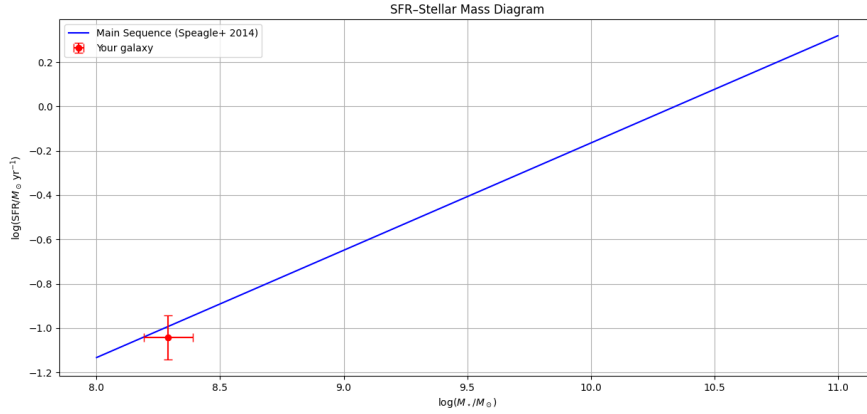


Figure 10: Star formation rate vs stellar mass for the galaxy, compared to the local main sequence from Speagle [10]. The red point indicates the position of the studied galaxy.

The uncertainties on both  $\log M_{\star}$  and  $\log \text{SFR}_{\text{H}\alpha}$  were estimated as follows. For the stellar mass, it was adopted an uncertainty of 0.1 dex, consistent with typical values reported in the literature for stellar population synthesis modelling based on medium-resolution spectra and photometry [7]. This value accounts for both fitting uncertainties and systematic effects related to assumptions on star formation history, metallicity, and dust attenuation. For the SFR derived from the narrow  $\text{H}\alpha$  component, it was applied an uncertainty of 0.1 dex to encompass the combined contribution from measurement errors in the line flux, absolute flux calibration uncertainties, and systematic uncertainties in the conversion from  $\text{H}\alpha$  luminosity to SFR due to IMF and extinction corrections [8]. These

uncertainties are shown by the red error bars in (Figure 10). Although the error on the SFR could in principle be propagated directly from the measured  $H\alpha$  flux uncertainty, we prefer this conservative approach to ensure that calibration and modeling contributions are included in the final error budget.

The position of the galaxy in the SFR–stellar mass diagram, Figure 10, is below the Main Sequence (MS) of the stellar mass. However, based on the error bars in both the stellar mass and the SFR measurements, the galaxy’s position is still consistent with the MS within uncertainties. Therefore, it remains uncertain whether the galaxy is undergoing significant suppression of star formation. This initial result is in agreement with the galaxy’s classification as an AGN host, in which active galactic nucleus feedback can plausibly stabilize or quench star formation, but more data would be needed to confirm such a transition

## 6 Discussion

### 6.1 Diagnostic Diagram Validation

The galaxy’s classification as an active galactic nucleus (AGN) is supported by multiple independent lines of evidence. The object is firmly located above the Kewley [5] demarcation curve on the BPT diagnostic diagram (Figure 6) and therefore in the AGN-dominated region. The measured emission line ratios,  $\log([O\ III]/H\beta) = 0.277$  and  $\log([N\ II]/H\alpha) = -0.082$ , indicate strong non-stellar ionisation sources.

Furthermore, the Gaussian decomposition of the  $H\alpha$  line profile (Figure 9) reveals a broad emission feature with  $FWHM \approx 3228\text{ km s}^{-1}$ , which is unambiguously associated with AGN-driven activity. Such broad components are rarely observed in purely star-forming systems and strongly support the presence of a Type 1 AGN.

The AGN nature is further reinforced by the high luminosity of the broad  $H\alpha$  component,  $L_{H\alpha, \text{broad}} = 4.14 \times 10^{42}\text{ ergs}^{-1}$ , and the corresponding black hole mass estimate of  $M_{BH} \approx 4.55 \times 10^7 M_{\odot}$ . These values are consistent with those observed in AGN at similar redshifts, typically around  $z \sim 2 - 4$  [14], although this reference does not focus exclusively on  $z = 3$ .

### 6.2 Physical Implications

The physical properties derived from the FADO [1] spectral synthesis and  $H\alpha$  emission analysis provide insight into the evolutionary state of the galaxy. The estimated stellar mass of  $\log M_{\star} = 8.29$  corresponds to a moderately low-mass system, while the instantaneous star formation rate,  $\log(SFR) \approx -1.04$ , is significantly lower than that expected for galaxies on the local main sequence of star formation.

When placed on the SFR– $M_{\star}$  plane (Figure 10), the galaxy lies below the empirical main sequence relation from Speagle [10]. This deviation is indicative of star formation quenching or suppression. Given the robust AGN classification, the most plausible explanation is that feedback mechanisms associated with the central supermassive black hole are actively inhibiting further star formation.

AGN-driven outflows, radiation pressure, and heating of the interstellar medium are all possible contributors to this suppression. Although no direct detection of outflows is presented here, the kinematic structure of the broad  $H\alpha$  component may hint at turbulent or dynamic processes consistent with AGN feedback. The low light-weighted age of the stellar populations ( $\langle \log t_{\star} \rangle_L = 8.78$ ) suggests relatively recent episodes of star formation.

Overall, the evidence points toward a galaxy in transition — previously forming stars actively, but now dominated by AGN activity that is likely regulating its further evolution toward a more passive phase.

## 7 Conclusion

It is here presented a multi-faceted analysis of a galaxy using spectral fitting, emission line diagnostics, and physical parameter inference. The galaxy is conclusively classified as an AGN through its placement on the BPT diagram and the detection of a broad  $H\alpha$  component with high FWHM and luminosity. Spectral synthesis via FADO [1] reveals a moderate stellar mass and a star formation rate well below the expected value for main-sequence galaxies.

The combination of a low SFR, AGN-like emission line ratios, and a broad Balmer line suggests that AGN feedback is actively suppressing star formation in this system. The galaxy appears to be undergoing a phase of transition, potentially moving from a star-forming state toward quiescence, mediated by the influence of its central black hole.

These results underscore the importance of AGN activity in regulating galaxy evolution, even in relatively low-mass systems at high redshift. Future higher-resolution investigations could help to map the scale of feedback processes and provide direct evidence of outflows.



A potential future line of investigation could be pursued into to the chemical enrichment properties to complement the current analysis.

**Acknowledgements:** I would like to express my gratitude to Professor Ciro Pappalardo for his wise advice during this research; to Henrique Miranda for his valuable input regarding work quality overall; to Thushara Sinnathamby for her help with coding and general support during the project; and to Mariana Rosado for her careful suggestions regarding the grammatical aspects of this paper.

## References

- [1] Gomes, J. M., & Papaderos, P. (2017). Fitting Analysis using Differential evolution Optimization (FADO): Spectral population synthesis through genetic optimization under self-consistency boundary conditions. *Astronomy & Astrophysics*, 603, A63. <https://doi.org/10.1051/0004-6361/201730885>
- [2] Cardelli, J. A., Clayton, G. C., & Mathis, J. S. (1989). The relationship between infrared, optical, and ultraviolet extinction. *The Astrophysical Journal*, 345, 245–256.
- [3] Charlot, S., & Fall, S. M. (2000). A Simple Model for the Absorption of Starlight by Dust in Galaxies. *The Astrophysical Journal*, 539(2), 718–731.
- [4] Calzetti, D., Armus, L., Bohlin, R. C., et al. (2000). The Dust Content and Opacity of Actively Star-forming Galaxies. *The Astrophysical Journal*, 533(2), 682–695.
- [5] Kewley, L. J., Dopita, M. A., Sutherland, R. S., Heisler, C. A., & Trevena, J. (2001). Theoretical Modeling of Starburst Galaxies. *The Astrophysical Journal*, 556(1), 121–140.
- [6] Kauffmann, G., Heckman, T. M., Tremonti, C., et al. (2003). The host galaxies of active galactic nuclei. *Monthly Notices of the Royal Astronomical Society*, 346(4), 1055–1077.
- [7] Miranda, H., Pappalardo, C., Papaderos, P., Afonso, J., Matute, I., Lobo, C., Paulino-Afonso, A., Carvajal, R., Lorenzoni, S., & Santos, D. 2022, *An investigation of the star-forming main sequence considering the nebular continuum emission at low-z*, arXiv:2212.02593
- [8] Kennicutt, R. C. 1998, *Star Formation in Galaxies Along the Hubble Sequence*, Annual Review of Astronomy and Astrophysics, 36, 189–232
- [9] Greene, J. E., & Ho, L. C. 2005, *Estimating Black Hole Masses in Active Galaxies Using the H $\alpha$  Emission Line*, The Astrophysical Journal, 630, 122–129
- [10] Speagle, J. S., Steinhardt, C. L., Capak, P. L., & Silverman, J. D. 2014, *A Highly Consistent Framework for the Evolution of the Star-forming “Main Sequence” from  $z \sim 0$  to  $z \sim 6$* , The Astrophysical Journal Supplement Series, 214(2), 15
- [11] Baldwin, J. A., Phillips, M. M., & Terlevich, R. 1981, *Classification parameters for the emission-line spectra of extragalactic objects*, Publications of the Astronomical Society of the Pacific, 93, 5
- [12] Finkelstein, S. L., Bagley, M., Dickinson, M., et al. 2023, *The CEERS Survey: First Data Release and Initial Results*, The Astrophysical Journal Supplement Series, 264, 22
- [13] Vestergaard, M., & Peterson, B. M. 2006, *Determining Central Black Hole Masses in Distant Active Galaxies*, The Astrophysical Journal, 641, 689
- [14] Shen, Y., Richards, G. T., Strauss, M. A., et al. 2011, *A Catalog of Quasar Properties from Sloan Digital Sky Survey Data Release 7*, The Astrophysical Journal Supplement Series, 194, 45
- [15] Rieke, M. J., Eisenstein, D. J., Egami, E., et al. 2023, *The JWST Advanced Deep Extragalactic Survey (JADES)*, The Astrophysical Journal Letters, 946, L13
- [16] Osterbrock, D. E., & Ferland, G. J. 2006, *Astrophysics of Gaseous Nebulae and Active Galactic Nuclei*, 2nd Edition, University Science Books
- [17] Porqueres, N., Jasche, J., Enßlin, T., & Lavaux, G. 2017, *Astronomy & Astrophysics*, 612, A40, [doi:10.1051/0004-6361/201732141](https://doi.org/10.1051/0004-6361/201732141), “Imprints of the large-scale structure on AGN formation and evolution”